

Excitonic Bose-polarons in electron-hole bilayers

E. A. Szwed, B. Vermilyea, D. J. Choksy, Zhiwen Zhou, M. M. Fogler, and L. V. Butov
Department of Physics, University of California San Diego, La Jolla, CA 92093, USA

D. K. Efimkin
School of Physics and Astronomy, Monash University, Victoria 3800, Australia

K. W. Baldwin and L. N. Pfeiffer
Department of Electrical Engineering, Princeton University, Princeton, NJ 08544, USA
 (Dated: June 25, 2024)

Bose polarons are mobile impurities dressed by density fluctuations of a surrounding degenerate Bose gas. These many-body objects have been realized in ultracold atomic gases and become a subject of intensive studies. In this work, we show that excitons in electron-hole bilayers offer new opportunities for exploring polarons in strongly interacting, highly tunable bosonic systems. We found that Bose polarons are formed by spatially direct excitons immersed in degenerate Bose gases of spatially indirect excitons (IXs). We detected both attractive and repulsive Bose polarons by measuring photoluminescence excitation spectra. We controlled the density of IX Bose gas by optical excitation and observed an enhancement of the energy splitting between attractive and repulsive Bose polarons with increasing IX density, in agreement with our theoretical calculations.

PACS numbers:

An impurity particle in a degenerate Bose or Fermi gas gets dressed by excitations of the surrounding medium, becoming, respectively, a Bose or Fermi polaron. Such polarons have been realized in ultracold atomic Bose [1–5] and Fermi [6–10] gases. A recent finding of excitonic Fermi polarons in degenerate electron gases in two-dimensional (2D) semiconductor heterostructures (HS) initiated intensive studies of these new quasiparticles [11–19]. Degenerate Bose gases of excitons [20] or exciton-polaritons [21] can serve as a medium for excitonic Bose polarons. In this work, we present experiments with electron-hole (e-h) bilayers in GaAs HS hosting two types of excitons: spatially indirect, or interlayer, excitons (IXs), and spatially direct, or intralayer, excitons (DXs), see Fig. 1a,b. The photo-excited DXs behave as polaronic impurities in a degenerate Bose gas of IXs, Fig. 1c. We observe spectroscopic signatures of two kinds of such polarons: attractive and repulsive Bose polarons (ABPs and RBPs, respectively). The ABPs are the stable low-energy polaron quasiparticles whereas RBPs are the long-lived excited states in the many-body continuum.

Semiconductor HS's containing e-h bilayers are suited for studying ultracold neutral e-h matter (Fig. 1a). The layer separation drastically increases e-h recombination lifetimes, which allows such systems to reach low-temperature quasi-equilibrium states even under optical excitation [22]. As summarized in Ref. [23], e-h bilayers can exhibit a variety of quantum phases, depending on the two key parameters: dimensionless density na_χ^2 and dimensionless layer separation d/a_χ . Here $a_\chi = \hbar^2\kappa/(\mu_{e-h}e^2)$ is the exciton Bohr radius, κ is the dielectric constant of the semiconductor, $\mu_{e-h} = (m_e^{-1} + m_h^{-1})^{-1}$ is

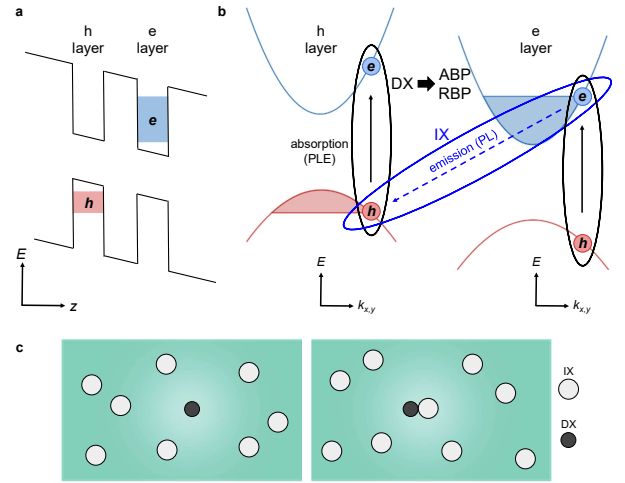


FIG. 1: Diagram of an electron-hole bilayer. (a) Electrons (e) and holes (h) are confined in separated layers. (b) Absorption (PLE) and emission (PL) in bilayer heterostructure. Spatially indirect excitons (IXs) and direct excitons (DXs) are shown by the ovals. (c) Free DXs (left) and DX-IX bound states (right) interact with surrounding IXs and form attractive and repulsive Bose polarons (ABP and RBP).

the reduced e-h mass, and m_e (m_h) is the electron (hole) effective mass. In our GaAs system $d = 19$ nm (center-to-center separation, Fig. 1a) is not much larger than $a_\chi \approx 13$ nm, so the most experimentally relevant phases are as follows. At low densities, $na_\chi^2 \ll 1$, electrons and holes form a Bose-Einstein condensate (BEC) of tightly bound, hydrogen-like IXs [24, 25]. At moderate densities, $na_\chi^2 \sim 1$, IXs become weakly bound and Cooper-

pair-like, so that the BEC crosses over to a Bardeen-Cooper-Schrieffer (BCS) state [26–28]. At high density, $na_X^2 \gg 1$, the IX binding energy is exponentially small (or perhaps, zero), so that the state of the system is best described as a correlated Fermi liquid of electrons and holes. These three regimes can be expressed as the condition on the energy scale

$$E_n = (\pi\hbar^2/\mu_{e-h})n, \quad (1)$$

which has the meaning of the Fermi edge, i.e., the sum of the Fermi energies of noninteracting electrons and holes. This quantity is much smaller, of the order of, and larger than the IX binding energy $E_{IX} \sim \hbar^2/\mu_{e-h}a_X^2$ in the BEC, BCS, and Fermi-liquid regimes, respectively.

The experiments were done with GaAs HS containing two 15 nm-thick quantum wells (QWs) separated by a 4 nm-wide AlGaAs barrier. Electrons and holes were optically generated and their density was controlled by the laser excitation power P_{ex} . Electrons and holes were driven into different QWs by an applied voltage (Fig. 1a). This significantly increased e-h recombination time, to $\tau \sim 1\mu s$, allowing the system to cool down and form the aforementioned quantum phases. Further details regarding the sample and the measurements are presented in Supplementary Information (SI).

Previous photoluminescence (PL) studies of this system [28] are consistent with the BEC-BCS crossover occurring with increasing P_{ex} . Here we study photoluminescence excitation (PLE) spectra. The PLE signal is a measure of optical absorption in the system. The absorption is dominated by spatially direct (intralayer) optical transitions, e.g., photoexcitation of DXs. Absorption via spatially indirect (interlayer) transitions is much weaker and is not observed. However, the DX density is always much smaller than the IX density due to a fast interlayer e-h relaxation and long IX lifetime [29]. The IX densities in the PLE experiments were estimated to be in the range $n = 0.3\text{--}11 \times 10^{10} \text{ cm}^{-2}$. These estimates are based on the measured blue shift δE of the IX PL energy and the ‘capacitor’ formula [30] $\delta E = (4\pi e^2 d/\kappa)n$, which becomes increasingly more accurate as n gets larger [29, 31].

Our principal finding is a set of peaks in the PLE spectra, which display a pronounced n -dependence. As labeled in Fig. 2a, we attribute the two lowest-energy peaks to ABP and RBP formed from DXs containing heavy holes (hh) and the next pair of peaks those containing light holes (lh). The photo-excited DXs behave as many-body objects dressed by excitations of the surrounding IX Bose gas. As the IX density increases, an approximately linear increase of the ABP and RBP energies (Fig. 2b) as well as their splitting $\Delta_{ABP-RBP}$ (Fig. 2c) is observed. This behavior is reproduced within a theoretical model (solid line in Fig. 2c) to be discussed at the end. This model treats the DX-IX interaction and phase-space filling [32] (PSF) effects in a unified fashion. According to this model, at low n the RBP evolves into a free DX

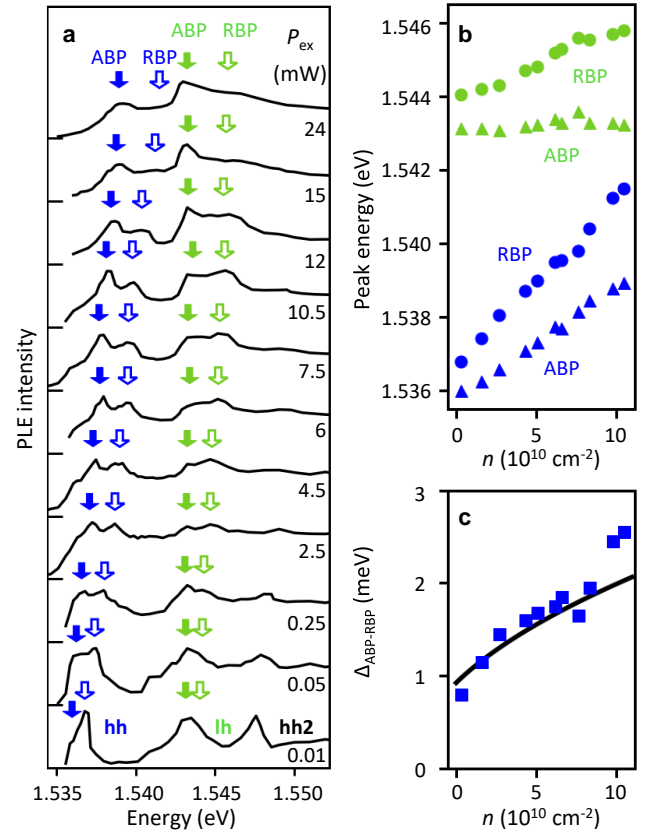


FIG. 2: Measured PLE spectra. (a) PLE spectra vs. the laser excitation power P_{ex} at both temperature $T = 2 \text{ K}$. The first two peaks in the order of increasing energy correspond to ABP and RBP for DXs containing heavy holes (hh). The next two peaks correspond to ABP and RBP for DXs containing light holes (lh). The higher-energy peaks originate from higher QW subbands. (b) Polaron energies vs. IX density (symbols). (c) Measured (squares) and calculated (line) ABP-RBP energy splitting for the hh DXs. The calculations [Eq. (5)] use the estimated $E_{XX} = (0.88 + 0.96)/2 = 0.92 \text{ meV}$ and $g_3 = 0.084 \times 10^{-10} \text{ meV cm}^{-2}$.

and the ABP into a DX-IX biexciton, so that the energy splitting $\Delta_{ABP-RBP}$ should approach the DX-IX biexciton binding energy E_{XX} . There are two possible biexciton types in our CQW, (h-e-h)(e) and (e-h-e)(h), where the parentheses group together particles residing in the same QW. The calculated $E_{XX} = 0.88$ and 0.96 meV for, respectively, (h-e-h)(e) and (e-h-e)(h) are close to the measured $\Delta_{ABP-RBP} = 0.8 \text{ meV}$, see Fig. 1c and Sec. IV in SI.

In Fig. 3 we compare two energy scales: the energy shift Δ_{PLE} of the lowest-energy ABP peak in the PLE spectra (Fig. 2a) and the spectral width Δ_{PL} of the PL line (Fig. 3b). We measure Δ_{PLE} with respect to the lowest-density ABP position 1.536 eV . At the higher densities, a shoulder is observed at this energy in the PLE spectra marking the onset of absorption. This shoulder is more pronounced at $P_{ex} = 2.5\text{--}7.5 \text{ mW}$ (Fig. 2a) and its position is nearly density independent. In turn, we define

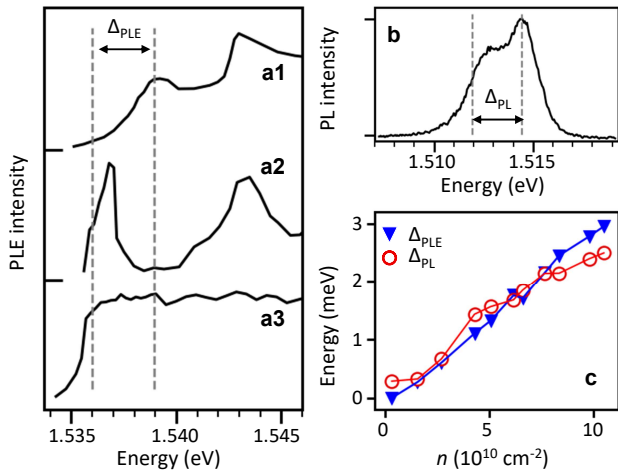


FIG. 3: PLE energy shift and PL energy width. (a) PLE spectra at $T = 2 \text{ K}$, $P_{\text{ex}} = 24 \text{ mW}$ (line a1); $T = 2 \text{ K}$, $P_{\text{ex}} = 0.01 \text{ mW}$ (line a2); $T = 20 \text{ K}$, $P_{\text{ex}} = 24 \text{ mW}$ (line a3). At high temperatures (line a3), the excitonic peaks have vanished and the spectrum has become step-like, corresponding to the density of states of a 2D e-h plasma. Δ_{PLE} denotes the shift of the hh-ABP line with increasing density. (b) PL spectrum at $T = 2 \text{ K}$, $P_{\text{ex}} = 24 \text{ mW}$, estimated e-h density $n = 1.1 \times 10^{11} \text{ cm}^{-2}$. The PL enhancement at the Fermi edge comes from Cooper-pair-like IXs [28]. Δ_{PL} is the PL energy of Cooper-pair like IX at the Fermi energy relative to the low-energy PL. (c) Δ_{PL} and Δ_{PLE} vs. IX density. $T = 2 \text{ K}$. The observed relation $\Delta_{\text{PLE}} \approx \Delta_{\text{PL}}$ indicates that the ABP energy shift is close to E_n .

Δ_{PL} as the distance from the shoulder on the low-energy side at half-maximum intensity and a peak on the high-energy side of the PL line (Fig. 3b). The peak appears at high enough densities and is a signature of Cooper-pair-like excitons (Fig. 3b) in the BCS phase [28]. Apart from that peak, the PL has the box-like shape expected for cold e-h plasma, so Δ_{PL} is approximately equal to the Fermi edge E_n . (We used this consideration to verify the accuracy of the capacitor formula for n .) Figure 3c indicates that Δ_{PLE} and Δ_{PL} nearly coincide in most of the studied density range. This implies that $\Delta_{\text{PLE}} \approx E_n$, i.e., the energy shift of the ABP peak is of the order of Fermi edge energy. As alluded to above, this energy shift comes from a combination of Coulomb interaction and PSF effects, see more at the end.

With increasing temperature, the quantum-degenerate Bose gas of IXs evolves into classical IX gas at low densities and e-h plasma at high densities, respectively. The ABP and RBP lines vanish and the PLE spectrum becomes step-like (Fig. 3, line a3). The step-like PLE and the box-like PL have the same origin: the density of states being flat in 2D. At high temperatures, the absorption edge in the dense e-h system drops in comparison to low temperatures (Fig. 3, lines a1 and a3), as expected for the reduction of the PSF

in a classical e-h gas [32].

At the highest e-h densities in our experiments, the Fermi edge energies E_n are above the IX binding energy $E_{\text{IX}} = 3 \text{ meV}$ (SI, Sec. IV) and, therefore, IXs are in the high-density regime. Still E_n are below the calculated DX binding energy $E_{\text{DX}} = 8\text{--}9 \text{ meV}$ (SI, Sec. IV), and so the polaron approach remains sensible.

We now discuss higher-energy peaks in the PLE spectra (Fig. 2a). We attribute the third and fourth peaks (in the order of increasing energy) to lh DXs. Indeed, at the lowest IX density, the separation $\sim 7 \text{ meV}$ between this pair of peaks and the first pair of peaks agrees with the calculated lh-hh splitting [33], see SI for details. At finite density, the lh DXs become Bose polarons and their ABP-RBP energy splitting increases with n similarly to the case of hh DXs (Fig. 2a,b). However, for lh lines the energy increase with n is slower than for the hh lines (Fig. 2a,b). This suggests that the PSF and Coulomb interaction effects are weaker for lh polarons compared to hh polarons when the hh IX states are occupied.

The PLE peaks seen at even higher energies originate from higher-order QW subbands. For instance, we assign the peak at 1.548 eV (Fig. 2a) to hh2, the heavy holes in the second subband. We do so because the splitting of approximately 12 meV of these peaks from the hh DX peaks (Fig. 2a) matches the calculated splitting between the hh and hh2 subbands in 15 nm QWs [33] (see also SI). The hh2 peaks disappear at relatively low densities (Fig. 2a) that limits their analysis.

Now we discuss our theoretical model of excitonic polarons. In this model, the ABP corresponds to the DX-IX biexciton dressed by excitations of the IX Bose gas while the RBP corresponds to a dressed free DX. Our numerical study of four-body systems (SI, Sec. IV) reveals that biexcitons are stable only in the symmetric channel, e.g., when the total spin of the two identical particles in the same layer [electrons for (e-h-e)(h) and holes for (e)(h-e-h)] is zero. Accordingly, at low IX densities n , we can treat DXs and IXs as composite bosons interacting via a short-range effective potential, which is binding in the symmetric and non-binding in the antisymmetric channel. At the mean-field level, the n -dependence of the polaron energies is linear: $E_{\text{RBP}}^{(0)}(n) = ng_1$, $E_{\text{ABP}}^{(0)}(n) = ng_2 - E_{\text{XX}}$. These energies are referenced to the bare DX energy. Parameter g_1 can be estimated within the Hartree-Fock approximation [32, 34, 36], which includes the Coulomb interaction and PSF effects to the lowest order and yields

$$ng_1 = 0.45E_n \quad (2)$$

for the hh case (SI, Sec. VII). We also expect $g_2 \approx g_1$, at least, away from ultralow density regime. The idea is that since the DX-IX biexciton is weakly bound, being ‘tethered’ to one of IXs does not affect the interaction of the DX with other IXs too much.

An improvement over the naive mean-field theory is the T -matrix approximation where the polariton energy is derived from the equation $E = \text{Re } \Sigma(E)$, with $\Sigma(E) = nT(E)$ being the DX self-energy [32, 35, 36]. The essential physics of the problem can be modelled by the T -matrix of the Fano-Feshbach form

$$T(E) = g_1 + g_3 \frac{E_{XX}}{E - E_{ABP}^{(0)}}. \quad (3)$$

We take g_i 's to be constant, thus neglecting any energy or momentum dependence of DX-IX scattering. We also assume them to be real, so we neglect the imaginary part of $T(E)$ and the corresponding broadening of the spectral lines as well. Parameter g_3 characterizes the width of the DX-IX bound-state resonance. Parameter g_1 , already introduced above, represents non-resonant DX-IX scattering. For $g_1 = g_2$ case this model predicts

$$E_{ABP,RBP} = ng_1 - \frac{1}{2}E_{XX} \pm \frac{1}{2}\Delta_{ABP-RBP}, \quad (4)$$

$$\Delta_{ABP-RBP} = \left(E_{XX}^2 + 4ng_3E_{XX}\right)^{1/2}. \quad (5)$$

Hence, the n -dependence of the energy splitting $\Delta_{ABP-RBP}$ is controlled by g_3 . For a quick estimate, we choose $g_3 = \hbar^2(\pi/2)(1/m + 1/m_{DX})$, which gives the correct residue of the pole in $T(E)$ in the limit $n \rightarrow 0$ (SI, Sec. V). With $m_{DX} = m \equiv m_e + m_h = 0.285m_0$ for the hh exciton mass we find $g_3 = 0.084 \times 10^{-10} \text{ meV cm}^2$. The corresponding $\Delta_{ABP-RBP}(n)$ is shown by the line in Fig. 2c. It agrees reasonably well with the experiment. Next, we find $g_1 = 0.21 \times 10^{-10} \text{ meV cm}^2$ from Eq. (2). In comparison, by fitting Eq. (4) to the two lower data sets in Fig. 2b, i.e., hh ABP and RBP, we obtained $g_1 = 0.34 \times 10^{-10} \text{ meV cm}^2$ (SI, Sec. VII). This level of agreement is rather good for such crude estimates.

As mentioned in the introduction, the Mott transition (or crossover) from the excitonic to the correlated e-h Fermi liquid regime is expected to occur in our system at high n . The corresponding transition from Bose to Fermi polarons may result, which can be an interesting topic for future work.

In summary, we presented spectroscopic evidence for excitonic Bose polarons in electron-hole bilayers. These polarons are many-body objects formed around spatially direct excitons in a degenerate Bose gas of spatially indirect excitons. The energy splitting between attractive and repulsive branches of the Bose polarons grows with the indirect exciton density. We interpreted this behavior within a theoretical model employing the estimated biexciton binding energy and exciton interaction parameters.

ACKNOWLEDGMENTS

We thank E. Demler, J. Levinsen, and M. Parish for discussions. The PLE studies were supported by DOE

Award DE-FG02-07ER46449, the PL studies by NSF Grant 1905478, and the heterostructure growth by Gordon and Betty Moore Foundation Grant GBMF9615 and NSF grant DMR 2011750.

REFERENCES

-
- [1] Ming-Guang Hu, Michael J. Van de Graaff, Dhruv Kedar, John P. Corson, Eric A. Cornell, Deborah S. Jin, Bose Polarons in the Strongly Interacting Regime, *Phys. Rev. Lett.* **117**, 055301 (2016).
 - [2] Nils B. Jørgensen, Lars Wacker, Kristoffer T. Skalmstang, Meera M. Parish, Jesper Levinsen, Rasmus S. Christensen, Georg M. Bruun, Jan J. Arlt, Observation of Attractive and Repulsive Polarons in a Bose-Einstein Condensate, *Phys. Rev. Lett.* **117**, 055302 (2016).
 - [3] F. Camargo, R. Schmidt, J.D. Whalen, R. Ding, G. Woehl, Jr., S. Yoshida, J. Burgdörfer, F.B. Dunning, H.R. Sadeghpour, E. Demler, T.C. Killian, Creation of Rydberg Polarons in a Bose Gas, *Phys. Rev. Lett.* **120**, 083401 (2018).
 - [4] Zoe Z. Yan, Yiqi Ni, Carsten Robens, Martin W. Zwierlein, Bose polarons near quantum criticality, *Science* **368**, 190 (2020).
 - [5] Magnus G. Skou, Thomas G. Skov, Nils B. Jørgensen, Kristian K. Nielsen, Arturo Camacho-Guardian, Thomas Pohl, Georg M. Bruun, Jan J. Arlt, Non-equilibrium quantum dynamics and formation of the Bose polaron, *Nat. Phys.* **17**, 731 (2021).
 - [6] André Schirotzek, Cheng-Hsun Wu, Ariel Sommer, Martin W. Zwierlein, Observation of Fermi Polarons in a Tunable Fermi Liquid of Ultracold Atoms, *Phys. Rev. Lett.* **102**, 230402 (2009).
 - [7] S. Nascimbène, N. Navon, K.J. Jiang, L. Tarruell, M. Teichmann, J. McKeever, F. Chevy, C. Salomon, Collective Oscillations of an Imbalanced Fermi Gas: Axial Compression Modes and Polaron Effective Mass, *Phys. Rev. Lett.* **103**, 170402 (2009).
 - [8] C. Kohstall, M. Zaccanti, M. Jag, A. Trenkwalder, P. Massignan, G.M. Bruun, F. Schreck, R. Grimm, Metastability and coherence of repulsive polarons in a strongly interacting Fermi mixture, *Nature* **485**, 615 (2012).
 - [9] Marco Koschorreck, Daniel Pertot, Enrico Vogt, Bernd Fröhlich, Michael Feld, Michael Köhl, Attractive and repulsive Fermi polarons in two dimensions, *Nature* **485**, 619 (2012).
 - [10] Marko Cetina, Michael Jag, Rianne S. Lous, Isabella Fritsche, Jook T.M. Walraven, Rudolf Grimm, Jesper Levinsen, Meera M. Parish, Richard Schmidt, Michael Knap, Eugene Demler, Ultrafast many-body interferometry of impurities coupled to a Fermi sea, *Science* **354**, 96 (2016).
 - [11] Meinrad Sidler, Patrick Back, Ovidiu Cotlet, Ajit Srivastava, Thomas Fink, Martin Kroner, Eugene Demler, Atac Imamoglu, Fermi polaron-polaritons in charge-tunable atomically thin semiconductors, *Nat. Phys.* **13**, 255 (2017).
 - [12] Dmitry K. Efimkin, Allan H. MacDonald, Many-body theory of trion absorption features in two-dimensional semi-

- conductors, *Phys. Rev. B* **95**, 035417 (2017).
- [13] Yia-Chung Chang, Shiue-Yuan Shiau, Monique Combescot, Crossover from trion-hole complex to exciton-polaron in n-doped two-dimensional semiconductor quantum wells, *Phys. Rev. B* **98**, 235203 (2018).
- [14] Christian Fey, Peter Schmelcher, Atac Imamoglu, Richard Schmidt, Theory of exciton-electron scattering in atomically thin semiconductors, *Phys. Rev. B* **101**, 195417 (2020).
- [15] M.M. Glazov, Optical properties of charged excitons in two-dimensional semiconductors, *J. Chem. Phys.* **153**, 034703 (2020).
- [16] Dmitry K. Efimkin, Emma K. Laird, Jesper Levinsen, Meera M. Parish, Allan H. MacDonald, Electron-exciton interactions in the exciton-polaron problem, *Phys. Rev. B* **103**, 075417 (2021).
- [17] A. Tiene, J. Levinsen, J. Keeling, M.M. Parish, F.M. Marchetti, Effect of fermion indistinguishability on optical absorption of doped two-dimensional semiconductors, *Phys. Rev. B* **105**, 125404 (2022).
- [18] Di Huang, Kevin Sampson, Yue Ni, Zhida Liu, Danfu Liang, Kenji Watanabe, Takashi Taniguchi, Hebin Li, Eric Martin, Jesper Levinsen, Meera M. Parish, Emanuel Tutuc, Dmitry K. Efimkin, Xiaoqin Li, Quantum Dynamics of Attractive and Repulsive Polarons in a Doped MoSe₂ Monolayer, *Phys. Rev. X* **13**, 011029 (2023).
- [19] J. Levinsen, F. M. Marchetti, J. Keeling, and M. M. Parish, Spectroscopic Signatures of Quantum Many-Body Correlations in Polariton Microcavities, *Phys. Rev. Lett.* **123**, 266401 (2019).
- [20] Ivan Amelio, N.D. Drummond, Eugene Demler, Richard Schmidt, Atac Imamoglu, Polaron spectroscopy of a bilayer excitonic insulator, *Phys. Rev. B* **107**, 155303 (2023).
- [21] Li Bing Tan, Oriana K. Diessel, Alexander Popert, Richard Schmidt, Atac Imamoglu, Martin Kroner, Bose Polaron Interactions in a Cavity-Coupled Monolayer Semiconductor, *Phys. Rev. X* **13**, 031036 (2023).
- [22] Y.E. Lozovik, V.I. Yudson, A new mechanism for superconductivity: pairing between spatially separated electrons and holes, *Sov. Phys. JETP* **44**, 389 (1976).
- [23] M.M. Fogler, L.V. Butov, K.S. Novoselov, High-temperature superfluidity with indirect excitons in van der Waals heterostructures, *Nat. Commun.* **5**, 4555 (2014).
- [24] L.V. Keldysh, A.N. Kozlov, Collective properties of excitons in semiconductors, *Sov. Phys. JETP* **27**, 521 (1968).
- [25] A.A. High, J.R. Leonard, A.T. Hammack, M.M. Fogler, L.V. Butov, A.V. Kavokin, K.L. Campman, A.C. Gossard, Spontaneous coherence in a cold exciton gas, *Nature* **483**, 584 (2012).
- [26] L.V. Keldysh, Yu.V. Kopaev, Possible instability of the semimetallic state toward Coulomb interaction, *Sov. Phys. Solid State* **6**, 2219 (1965).
- [27] C. Comte, P. Nozières, Exciton Bose condensation: the ground state of an electron-hole gas - I. Mean field description of a simplified model, *J. de Physique* **43**, 1069 (1982).
- [28] D.J. Choksy, E.A. Szwed, L.V. Butov, K.W. Baldwin, L.N. Pfeiffer, Fermi edge singularity in neutral electron-hole system, *Nat. Phys.* **19**, 1275 (2023).
- [29] D.J. Choksy, Chao Xu, M.M. Fogler, L.V. Butov, J. Norman, A.C. Gossard, Attractive and repulsive dipolar interaction in bilayers of indirect excitons, *Phys. Rev. B* **103**, 045126 (2021).
- [30] D. Yoshioka, A.H. MacDonald, Double quantum well electron-hole systems in strong magnetic fields, *J. Phys. Soc. Jpn.* **59**, 4211 (1990).
- [31] Chao Xu, Michael M. Fogler, Ground and excited states of coupled exciton liquids in electron-hole quadrilayers, *Phys. Rev. B* **104**, 195430 (2021).
- [32] S. Schmitt-Rink, D.S. Chemla, D.A.B. Miller, Linear and nonlinear optical properties of semiconductor quantum wells, *Adv. Phys.* **38**, 89 (1989).
- [33] G. Bastard, J.A. Brum, Electronic states in semiconductor heterostructures, *IEEE J. Quant. Electron.* **22**, 1625 (1986).
- [34] C. Ciuti, V. Savona, C. Piermarocchi, A. Quattropani, P. Schwendimann, Role of the exchange of carriers in elastic exciton-exciton scattering in quantum wells, *Phys. Rev. B* **58**, 7926 (1998).
- [35] H. Haug, S. Schmitt-Rink, Electron theory of the optical properties of laser-excited semiconductors, *Progress in Quantum Electronics* **9**, 3 (1984).
- [36] Christoph Schindler and R. Zimmermann, Analysis of the exciton-exciton interaction in semiconductor quantum wells, *Phys. Rev. B* **78**, 045313 (2008).

Supporting Information for “Excitonic Bose-polarons in electron-hole bilayers”

E. A. Szwed, B. Vermilyea, D. J. Choksy, Zhiwen Zhou, M. M. Fogler, and L. V. Butov
Department of Physics, University of California San Diego, La Jolla, CA 92093, USA

D. K. Efimkin
School of Physics and Astronomy, Monash University, Victoria 3800, Australia

K. W. Baldwin and L. N. Pfeiffer
Department of Electrical Engineering, Princeton University, Princeton, NJ 08544, USA
(Dated: June 25, 2024)

I. SAMPLE

The sample used in this study is a coupled quantum well (CQW) heterostructure grown by molecular beam epitaxy. The CQW consists of two 15-nm-wide GaAs QWs separated by a 4-nm-thick $\text{Al}_{0.33}\text{Ga}_{0.67}\text{As}$ barrier. An n^+ GaAs layer with $n_{\text{Si}} \sim 10^{18} \text{ cm}^{-3}$ serves as a uniform bottom gate. The CQW is positioned 100 nm above the n^+ GaAs layer within the undoped 1- μm -thick $\text{Al}_{0.33}\text{Ga}_{0.67}\text{As}$ layer. The CQW is located much closer to the bottom gate to minimize the effect of fringing electric fields in excitonic devices with patterned top gates [1]. The top semi-transparent gate is fabricated by applying 2 nm of Ti and 7 nm of Pt on a 7.5 nm-thick GaAs cap layer. Applied gate voltage $V_g = -2.5 \text{ V}$ creates an electric field in the direction normal to the quantum wells. The corresponding band diagram of the CQW is shown in Fig. 1a of the main text. The applied voltage drives optically generated electrons (e) and holes (h) to the opposite quantum wells. This process is fast, so that the densities of minority particles (e’s in the h-layer and h’s in the e-layer) are orders of magnitude smaller than the densities of majority particles (e’s in the e-layer and h’s in the h-layer).

II. OPTICAL MEASUREMENTS DETAILS

The PLE spectra (Fig. S1) probe spatially direct optical absorption within each QW. A spatially indirect absorption is much weaker and is not observed in PLE. The PL and PLE were measured $\sim 50 \mu\text{m}$ away from the laser excitation spot and $\sim 300 \text{ ns}$ after the excitation pulse, where a cold and dense e-h system of temperature close to the lattice temperature was formed [2]. To facilitate comparison with prior PL measurements [2], we use similar optical excitation and detection protocol, as follows. The e-h system is generated by a Ti:Sapphire laser. An acousto-optic modulator is used for making laser pulses (800 ns on, 400 ns off). A laser excitation spot with a mesa-shaped intensity profile and diameter $\sim 100 \mu\text{m}$ is created using an axicon. The signal is detected within a 50 ns window, which is much shorter than the IX lifetime, so that the signal variation during

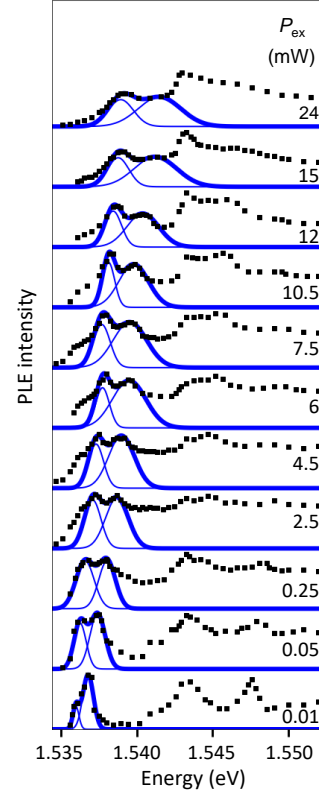


FIG. S1. Gaussian fits to the ABP and RBP peaks in the measured PLE spectra (points, same as Fig. 2a of the main text). The individual fits are shown by the thin lines and their sum by the thick line. The peak energies found from the fits are presented in Fig. 2b of the main text.

the measurement remains negligible [2]. The exciton density in the detection region is close to the density in the excitation spot because the separation is shorter than the IX propagation length and the time delay is shorter than the IX lifetime [2]. The IX PL spectra are measured using a spectrometer with resolution 0.2 meV and a liquid-nitrogen-cooled CCD coupled to a PicoStar HR TauTec time-gated intensifier. The experiments are performed in a variable-temperature ^4He cryostat.

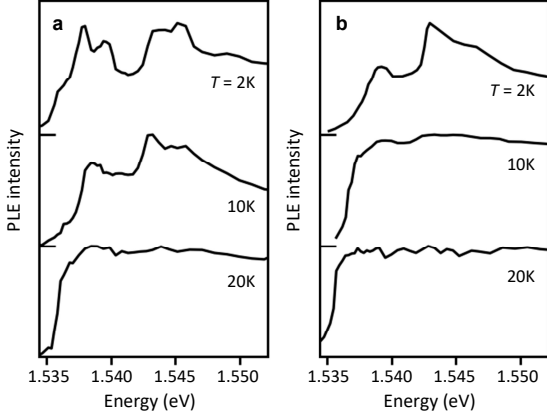


FIG. S2. PLE spectra at $P_{\text{ex}} = 7.5$ (a) and 24 (b) mW at $T = 2, 10,$ and 20 K. At high temperatures, the excitonic peaks vanish and the PLE spectrum becomes step-like as 2D density of states.

III. PLE SPECTRA

We used Gaussian fits for rough estimates of the ABP and RBP peak energies (Fig. S1). The actual ABP and RBP PLE lineshapes are complicated. In particular, their low-energy sides appearing near 1.536 eV have a non-Gaussian shoulder-like form (Fig. S1). The analysis of the lh-ABP and lh-RBP lines is also challenging because they appear on a background of optical transitions between free heavy holes and electrons, see the main text. Nevertheless, the variation of all the observed polaron energies with density are sufficiently strong and systematic (Fig. 2 of the main text). We note that the fit accuracy is lower for the highest P_{ex} , in particular, due to the RBP peak broadening.

With increasing temperature, the ABP and RBP lines vanish and the PLE spectrum becomes step-like, reflecting the functional form of the e-h joint density of states in 2D (Fig. S2). At high temperatures, the absorption edge in the dense e-h system decreases compared to the low-temperature data (Fig. S2), as discussed in the main text.

IV. EXCITON BINDING ENERGIES

Few-body e-h bound states that can form in the CQW are listed in Table SI, together with their calculated binding energies. They include indirect excitons (IXs), direct excitons (DXs), and DX-IX biexcitons. The details of the calculations are presented below.

The first step of the calculation is to solve for the single-particle states of the QWs. The electron states were determined from the Hamiltonian

$$H_e = \frac{1}{2m_e} \mathbf{P}^2 + U_e(z), \quad (\text{S1})$$

Complex	QW 1	QW 2	$h = \text{hh}$	$h = \text{lh}$
IX	e	hh	2.99	
DX	e-h		8.24	9.44
DX-IX	e-h-e	hh	0.96	1.26
DX-IX	e	h-e-hh	0.88	0.73

TABLE SI. Calculated binding energies of various e-h complexes, in units of meV, for zero gate voltage $V_g = 0$; ‘hh’ and ‘lh’ stand for the heavy hole and light hole, respectively.

where z is the coordinate perpendicular to the QW plane, $\mathbf{P} = (\mathbf{p}, -i\hbar\partial_z)$ is the momentum operator, $\mathbf{p} = \hbar\mathbf{k}_\perp$ is the in-plane momentum, and $m_e = 0.0665m_0$ is the effective electron mass in GaAs. The hole states were determined from the Hamiltonian [3, 4]

$$H_h = -\frac{1}{2m_0} \sum_{ij} P_i D_{ij} P_j + U_h(z), \quad (\text{S2})$$

$$\hat{D}_{ij} = \left(\frac{1}{2}\gamma_1 + \frac{5}{4}\gamma_2 \right) \delta_{ij} - \gamma_2 J_i J_j,$$

where γ_1 and γ_2 are the Luttinger parameters, m_0 is the free electron mass, and $\mathbf{J} = (J_x, J_y, J_z)$ is the spin-3/2 angular momentum operator. The confining potentials $U_e(z)$ and $U_h(z)$ were chosen in the form

$$U_{e,h}(z) = \begin{cases} 0 & \text{inside QW,} \\ U_{e,h} & \text{outside QW.} \end{cases} \quad (\text{S3})$$

For all the parameter values in our calculations we used those given in Ref. 5. We numerically diagonalized the Hamiltonians in Eqs. (S1) and (S2) and obtained the energy levels and wavefunctions $\varphi_i(z)$ where $i = e(h)n$ for e(h) states of QW $n = 1, 2$. The energy-momentum dispersions of the first three hole subbands are plotted in Fig. S3. To facilitate comparison with published results [3, 4] (that appears to be good) the momentum on the horizontal axis is expressed in units of $\pi \times 10^6 \text{ cm}^{-1}$.

Next, to define the effective mass m_h of the heavy hole (hh), we fitted its dispersion to a parabola over a range of momenta $0 < k_\perp < a_X^{-1}$, where $a_X = (\kappa\hbar^2/e^2)(m_e^{-1} + m_h^{-1})$ is again the exciton Bohr radius. We found $m_h = 0.217m_0 = 3.26m_e$, so that $a_X = 12.7 \text{ nm}$. Note that a_X^{-1} is about 0.25 in the momentum units used in Fig. S3. The light hole (lh) dispersion is non-monotonic. For simplicity, we decided to neglect this dispersion altogether, i.e., to treat the lh mass as infinite.

To compute the binding energies of interest we approximated the momentum-space Coulomb interaction potential between particles of charge e_i and e_j by

$$\tilde{V}_{ij}(\mathbf{k}_\perp) = \frac{2\pi e_i e_j}{\kappa k_\perp} \int dz dz' |\varphi_i(z)|^2 |\varphi_j(z')|^2 e^{-k_\perp |z-z'|}, \quad (\text{S4})$$

which we further simplified as follows. For particles in

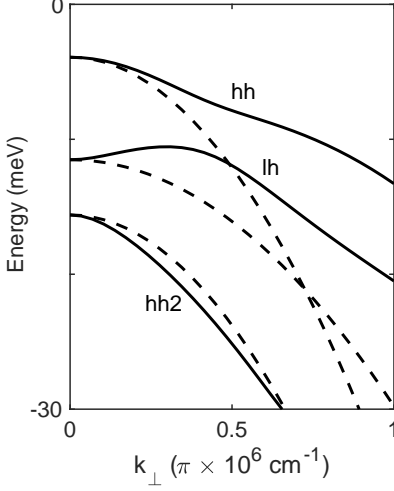


FIG. S3. In-plane dispersion $\varepsilon_h(\mathbf{k}_\perp)$ for the first three hole subbands in units of meV. The dashed lines are the dispersions obtained by neglecting the coupling between heavy and light holes (the off-diagonal terms of H_h).

the same layer, we used [4]

$$\tilde{V}_{ij}(\mathbf{k}_\perp) = \frac{2\pi e_i e_j}{\kappa k_\perp} \frac{1}{1 + k_\perp \rho_{ij}}, \quad (\text{S5a})$$

$$V_{ij}(\mathbf{r}) = \frac{\pi}{2\rho_{ij}} \frac{e_i e_j}{\kappa} \left[\mathbf{H}_0\left(\frac{r}{\rho_{ij}}\right) - Y_0\left(\frac{r}{\rho_{ij}}\right) \right], \quad (\text{S5b})$$

where the effective well widths $\rho_{en,en} = 4.5$ nm, $\rho_{hn,hn} = 3.81$ nm, and $\rho_{en,hn} = 4.17$ nm (all for hh), were determined by numerically evaluating the integrals in Eq. (S4) and fitting the result to Eq. (S5a) at $0 < k_\perp < a_X^{-1}$. Equation (S5b) is known as the Rytova-Keldysh potential. This function approaches the Coulomb potential $e_i e_j / \kappa r$ at $r \gg \rho_{ij}$ and diverges logarithmically $(e_i e_j / \kappa \rho_{ij}) \ln(\rho_{ij}/r)$ at $r \ll \rho_{ij}$; $\mathbf{H}_0(z)$ and $Y_0(z)$ are the Struve and Neumann functions, respectively.

For particles in opposite layers, we used $\rho_{ij} = 0$, i.e., the Coulomb law:

$$\tilde{V}_{ij}(\mathbf{k}_\perp) = 2\pi \frac{e_i e_j}{\kappa k_\perp} e^{-k_\perp d}, \quad (\text{S6a})$$

$$V_{ij}(\mathbf{r}) = \frac{e_i e_j}{\kappa} \frac{1}{\sqrt{r^2 + d^2}}, \quad (\text{S6b})$$

where $d = 19$ nm is the center-to-center layer distance. These interlayer and intralayer potentials are plotted in Fig. S4. We neglected intersubband mixing because the energy separation between the subbands is relatively large, 5–7 meV, see Fig. S3.

We computed the DX and IX binding energies E_X and ground-state wavefunctions $\phi_X(\mathbf{k}_\perp)$ by numerically solv-

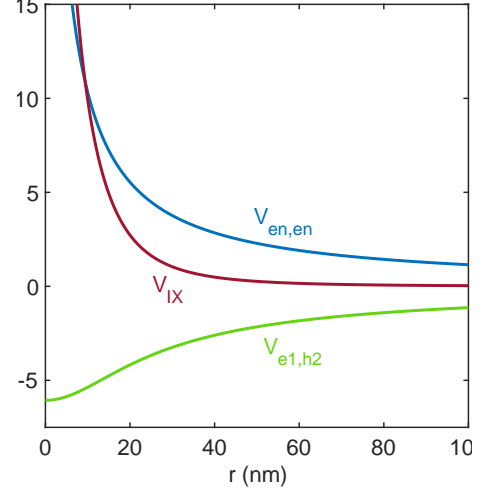


FIG. S4. Model interaction potentials: intralayer potential $V_{en,en} = V_{hn,hn}$ [Eq. (S5b)], interlayer potential $V_{e1,h2}$ [Eq. (S6b)], and the IX-IX potential V_{IX} [Eq. (S11)].

ing the Wannier equation,

$$[\varepsilon_e(\mathbf{k}_\perp) + \varepsilon_h(\mathbf{k}_\perp)]\phi_X(\mathbf{k}_\perp) + \Omega^{-1} \sum_{\mathbf{k}'_\perp} \tilde{V}_{ek,hn}(\mathbf{k}_\perp - \mathbf{k}'_\perp)\phi_X(\mathbf{k}'_\perp) = -E_X \phi_X(\mathbf{k}_\perp) \quad (\text{S7})$$

following Ref. 6. Here $X \in \{\text{DX}, \text{IX}\}$ is the exciton type, $\varepsilon_{e,h}(\mathbf{k}_\perp) = \hbar^2 \mathbf{k}_\perp^2 / 2m_{e,h}$ are the e(h) dispersions, and Ω is the area of the system.

Finally, we calculated the biexciton binding energies using the stochastic variational method (SVM), a highly accurate numerical technique for solving few-body quantum mechanics problems [7]. To this end we adopted the SVM code previously developed [8] for zero-thickness 2D layers ($\rho_{ij} \equiv 0$) and modified it to work with the interaction potential of Eq. (S5). We also used the SVM solver to verify the exciton binding energies E_X computed by the diagonalization method and found them to be in excellent agreement. Table SI summarizes the results for all the binding energies we calculated.

V. EXCITON-EXCITON INTERACTION

A. IX-IX interaction

Theoretical investigations of Bose polarons have been stimulated primarily by experiments with cold atoms. Transferring these methods to excitons must be done with caution because of important differences between two classes of systems. Atoms reach quantum degeneracy at very low temperatures in the nK or μK -

range. Since IXs have much smaller mass, their degeneracy temperature $T_{\text{deg}} = 2\pi T_0$ with $T_0 \equiv \hbar^2 n/m$ [9] is many orders of magnitude higher, e.g., $T_{\text{deg}} = 20$ K for $m = m_e + m_h = 0.285m_0$ and $n = 10^{11} \text{ cm}^{-2}$.

Atoms typically form dilute, weakly nonideal BECs (Bose-Einstein condensates) for which the details of the interatomic interaction potential are unimportant. Instead, the interactions are parametrized by the s -wave scattering amplitude, which is proportional to the on-shell two-body T -matrix. In 2D, this T -matrix has a universal low-energy form

$$T(E) \simeq \frac{4\pi\hbar^2}{m} \left[\ln \left(-\frac{\hbar^2}{ma^2} \frac{1}{E} \right) \right]^{-1}, \quad E \rightarrow 0, \quad (\text{S8})$$

where a is referred to as the scattering length. The T -matrix enters in equations for many key quantities of the system. For example, the chemical potential ζ of the BEC is given by

$$\zeta = Tn \quad (\text{S9})$$

to the leading order in $na^2 \ll 1$. In this equation, T needs to be evaluated at energy $E \sim -\zeta$ [10, 11], so that Eq. (S9) is a self-consistent equation for ζ as a function of n . The solution can be presented in the form

$$\tilde{g} \equiv \frac{\zeta}{T_0} = \frac{m}{\hbar^2} \frac{\zeta}{n} \simeq \frac{4\pi}{\ln(1/na^2)}. \quad (\text{S10})$$

The dimensionless parameter \tilde{g} is a measure of BEC nonideality. For example, it determines the interaction-induced condensate depletion via $\tilde{g}/(2\pi)$ [11]. These formulas apply if $\tilde{g} \lesssim 1$ [12, 13], which translates to the condition on the boson density $na^2 \lesssim 10^{-6}$. Despite the small numerical factor on the right-hand side of this inequality, it is not uncommon to have it fulfilled for cold atoms. In contrast, such densities are unrealistically low for IXs in GaAs heterostructures. As a result, scattering length a is not useful for describing these excitonic systems. Their properties crucially depend on details of the IX-IX interaction and they are typically strongly coupled, $\tilde{g} \gg 1$.

One common model for the interaction potential of two IXs is

$$V_{\text{IX}}(r) = V_{\text{ee}}(r) + V_{\text{hh}}(r) + 2V_{\text{eh}}(r), \quad (\text{S11})$$

where r is the distance between the centers of mass of the IXs. As one can see from Fig. S4, potential $V_{\text{IX}}(r)$ has a strong repulsive core and rapidly decreasing tails. Equation (S11) is essentially classical, e.g., it neglects fermionic and bosonic exchange of IXs [14] at distances $r \lesssim a_X$. However, due to the strong IX-IX repulsion [8, 15], excitons tend to avoid each other and these exchange effects should be small at densities $n \ll a_X^{-2} \sim 6 \times 10^{11} \text{ cm}^{-2}$ studied in our experiments.

At $r \gg d$, the IX-IX potential approaches $V_{\text{IX}}(r) \simeq e^2 d^2 / \kappa r^3$. The corresponding s -wave scattering length a

is given by [13] $a = e^{2\gamma_E} d^2 / A_X$, where $\gamma_E = 0.577$ is the Euler constant and $A_X = \hbar^2 \kappa / m e^2 = 2.3 \text{ nm}$. For $d = 19 \text{ nm}$, we find $a = 500 \text{ nm}$, so that in our experiments $na^2 \gg 1$. In this regime Eq. (S10) fails and is replaced by

$$\tilde{g} \equiv \frac{m}{\hbar^2} \frac{\zeta}{n} = \begin{cases} C_g \sqrt{na^2}, & n \ll 1/d^2, \\ 4\pi e^{-2\gamma_E} \frac{a}{d}, & n \gg 1/d^2, \end{cases} \quad (\text{S12a})$$

$$\tilde{g} \equiv \frac{m}{\hbar^2} \frac{\zeta}{n} = \begin{cases} C_g \sqrt{na^2}, & n \ll 1/d^2, \\ 4\pi e^{-2\gamma_E} \frac{a}{d}, & n \gg 1/d^2, \end{cases} \quad (\text{S12b})$$

which is specific to the interaction law (S11). The numerical constant $C_g \sim 5$ in Eq. (S12a) can be estimated from Ref. [16] and work cited therein. Note that Eq. (S12b) is the same as the ‘capacitor formula’ introduced in the main text. From these equations, we find $\zeta \sim 30\text{--}300 \text{ K}$, $T_0 \sim 0.3\text{--}3 \text{ K}$, and $\tilde{g} \sim 40\text{--}80$ in our experiments, indicating that IXs form a strongly correlated Bose gas rather than a weakly nonideal BEC. The large value of \tilde{g} is not a cause for concern; it simply shows that the s -wave scattering length a is not a meaningful control parameter for such dense many-body systems.

B. DX-IX interaction

The interaction between impurities and host bosons in cold atom gases and in excitonic systems also has some qualitative differences. In the context of cold atoms it is common to describe this interaction using another parameter of dimension of length — the size of the impurity-host dimer. If this length is much larger than the scattering length a of the host bosons, the impurity can attract many host particles. As a result, the ABP becomes a multi-particle cluster with energy much lower than the dimer energy [17]. A related effect is formation of multimers (trimers, quadrimers, *etc.*) in a few-body bosonic systems [18]. In our case, the size of the DX-IX bound state, defined by the relation

$$a_{\text{XX}} = \frac{\hbar}{(2\mu E_{\text{XX}})^{1/2}} \approx 15 \text{ nm}, \quad (\text{S13})$$

is much smaller than the IX-IX scattering length $a \approx 500 \text{ nm}$. [Here $\mu = (m_{\text{DX}}^{-1} + m^{-1})^{-1}$ is the reduced mass of DX and IX, m is the IX mass, and m_{DX} is the DX mass. We used $E_{\text{XX}} = 1.11 \text{ meV}$, which is the average of the hh and lh values in Table S1.] This means that the IX-IX repulsion is strong compared to the DX-IX attraction. Therefore no multimers or multi-exciton clusters can appear and the excitonic ABP is essentially a dimer.

As mentioned in the main text, the DX-IX bound states, e.g., (e-h-e)(h) biexcitons, which Eq. (S13) refers to, are stable only when the spins on the two e’s form a singlet. The spin dependence of the interaction of the excitons comes from the symmetries of their orbital wavefunctions. It indicates that exchange plays an important role in the DX-IX interaction unlike the case of the IX-IX interaction discussed in Sec. VA above.

The exchange effects can be analyzed as follows. Taking the (e-h-e)(h) complex as an example, we note that in

GaAs each of the four particles involved can exist in two spin states, $s_z = \pm 1/2$ for the e's and $J_z = \pm 3/2$ for the h's, yielding $2^4 = 16$ combinations total. In this Hilbert space we can select a basis of spin wavefunctions that are either even or odd with respect to interchange of e's or h's. The corresponding orbital wavefunctions must have the opposite parity and therefore different scattering amplitudes. Following Ref. [15], we can describe the DX-IX interaction using four different T -matrices T_v^u , where u and v refer to e and h, respectively, $u, v \in \{s, a\}$ and $s(a)$ indicates symmetric (antisymmetric) orbital wavefunction. The $u = v = s$ channel is a singlet. The spin degeneracy triples if u or v is switched from s to a , so that the original 16-fold degeneracy is split into four channels of spin degeneracy 1, 3, 3, and 9. In the present case, the problem is actually simpler because we can neglect exchange between particles residing in different QWs, e.g., the h-exchange in the (e-h-e)(h) DX-IX complex. Thus, we can disregard the spin of the two h's. We need to consider only the four e-spin states that split into an antisymmetric triplet, described by a T -matrix $T_a^a = T_s^a \equiv T^a$ and a symmetric singlet, characterized by another T -matrix $T_a^s = T_s^s \equiv T^s$.

Some properties of these T -matrices are known from general principles. The triplet channel is non-binding, the singlet channel supports bound state(s). Therefore, $T^a(E)$ is analytic at all negative energies $E < 0$ whereas $T^s(E)$ has a pole at $E = -E_{XX}$. In the asymptotic low-energy limit $E \rightarrow 0$, both T^a and T^s have the universal form [cf. Eq. (S8)]

$$T^u(E) = \frac{\tilde{V}^u}{1 - L(E)\tilde{V}^u}, \quad (\text{S14})$$

$$L(E) = \frac{1}{\Omega} \sum_{|\mathbf{k}| < \Lambda} \frac{1}{E - \varepsilon_{\mathbf{k}} - \varepsilon_{\text{DX},\mathbf{k}}} \simeq -\frac{\mu}{2\pi\hbar^2} \ln\left(-\frac{\hbar^2\Lambda^2}{2\mu E}\right). \quad (\text{S15})$$

This expression represents the sum of all ladder diagrams for two particles — an IX with dispersion $\varepsilon_{\mathbf{k}} = \hbar^2\mathbf{k}^2/2m$ and a DX with dispersion $\varepsilon_{\text{DX},\mathbf{k}} = \hbar^2\mathbf{k}^2/2m_{\text{DX}}$ — interacting via a short-range effective potential $V^u(r)$ such that $\tilde{V}^a > 0$ and $\tilde{V}^s < 0$. Parameter $\Lambda \sim a_X^{-1}$ is the high-momentum cutoff. If the binding energy E_{XX} belongs to the range of validity of Eq. (S14), then \tilde{V}^s can be deduced from the condition that $T^s(E)$ has a pole at $E = -E_{XX}$:

$$\tilde{V}^s = -\frac{\hbar^2}{\mu} \frac{\pi}{\ln(\Lambda a_{XX})}, \quad (\text{S16})$$

which entails

$$\begin{aligned} T^s(E) &= \frac{2\pi\hbar^2}{\mu} \left[\ln\left(-\frac{E_{XX}}{E}\right) \right]^{-1} \\ &\simeq \frac{2\pi\hbar^2}{\mu} \frac{E_{XX}}{E + E_{XX}}, \quad E \rightarrow -E_{XX}. \end{aligned} \quad (\text{S17})$$

Accurate calculation of T^a and T^s at arbitrary energies and momenta requires solving the four-body scattering problem numerically, which goes beyond the scope of the present work. (Currently, our numerical codes can only solve for the bound states, see Sec. IV.) However, we can estimate T^a and T^s by combining Eqs. (S14), (S15) with the Hartree-Fock approximation for $\tilde{V}^{a(s)} = \tilde{V}_d \pm \tilde{V}_x$ [14, 15, 19]. Due to the exciton charge neutrality, the Hartree (or direct) term \tilde{V}_d is negligible compared to the Fock (or e-exchange) term \tilde{V}_x , so that

$$T^{a(s)}(E) \approx \pm \frac{\tilde{V}_x}{1 \mp L(E)\tilde{V}_x}. \quad (\text{S18})$$

The equation for the Fock term is

$$\begin{aligned} \tilde{V}_x &= - \int \frac{d^2k}{(2\pi)^2} \int \frac{d^2k'}{(2\pi)^2} W(\mathbf{k}, \mathbf{k}'), \\ W(\mathbf{k}, \mathbf{k}') &= \tilde{V}_{e1,e1}(\mathbf{k} - \mathbf{k}')\Phi(\mathbf{k}, \mathbf{k}'; \mathbf{k}, \mathbf{k}') \\ &\quad + \tilde{V}_{e1,h2}(\mathbf{k} - \mathbf{k}')\Phi(\mathbf{k}, \mathbf{k}; \mathbf{k}, \mathbf{k}') \\ &\quad + \tilde{V}_{h1,e1}(\mathbf{k} - \mathbf{k}')\Phi(\mathbf{k}, \mathbf{k}; \mathbf{k}', \mathbf{k}) \\ &\quad + \tilde{V}_{h1,h2}(\mathbf{k} - \mathbf{k}')\Phi(\mathbf{k}, \mathbf{k}'; \mathbf{k}', \mathbf{k}), \end{aligned} \quad (\text{S19})$$

where

$$\Phi(\mathbf{k}, \mathbf{q}; \mathbf{k}', \mathbf{q}') \equiv \phi_{\text{DX}}^*(\mathbf{k})\phi_{\text{IX}}^*(\mathbf{q})\phi_{\text{DX}}(\mathbf{k}')\phi_{\text{IX}}(\mathbf{q}'). \quad (\text{S20})$$

For comparison with previous work, we can write

$$\tilde{V}_x = C_x \frac{\hbar^2}{2\mu_{e-h}}, \quad \frac{1}{\mu_{e-h}} \equiv \frac{1}{m_e} + \frac{1}{m_h}. \quad (\text{S21})$$

Using $\phi_{\text{DX}}(\mathbf{k})$, $\phi_{\text{IX}}(\mathbf{k})$ found as described in Sec. IV, we obtained the numerical coefficients $C_x = 3.81$ for hh and 3.24 for lh. Interestingly, they are only slightly larger than the analytical result $C_x = 4\pi - (315\pi^3/1024) = 3.03$ for the DX-DX interaction in a zero-thickness QW [19]. In physical units, we find

$$\tilde{V}_x = 0.28 \times 10^{-10} \text{ meV cm}^2 \quad (\text{S22})$$

for (e-h-e)(h) with $h = \text{hh}$.

At this point we can compare the Hartree-Fock estimate $\tilde{V}^s \approx -\tilde{V}_x$ with Eq. (S16). In fact, we can get them to agree perfectly by fixing the numerical factor in the momentum cutoff parameter, making the 'large logarithm' in Eq. (S16) equal to $\ln(\Lambda a_{XX}) = 0.59$, which corresponds to $\Lambda = 1.5/a_X$. With this adjustment, Eq. (S17) for T^s reproduces the accurate value of the binding energy $E_{XX} = 0.96 \text{ meV}$ in Table SI. It may now be tempting to use Eq. (S18) for \tilde{T}^a with the same Λ . However, doing so would generate a spurious pole in $\tilde{T}^a(E)$ at a relatively small (by absolute value) energy

$$E = -\left(\frac{\hbar^2\Lambda^2}{2\mu}\right) \frac{1}{E_{XX}} \approx -10 \text{ meV}. \quad (\text{S23})$$

We believe it is a sign of going beyond the range of validity of the approximation. Therefore, it may be better to revert to the lowest-order perturbation theory formula

$$T^a(E) = \widetilde{V}_x = \text{const.} \quad (\text{S24})$$

We take Eqs. (S17), (S22), and (S24) for two-body DX-IX scattering as the basis for the further analysis of the many-body Bose polaron problem in Sec. VII.

VI. BOSE POLARONS IN WEAKLY INTERACTING 2D SYSTEMS

There have been numerous theoretical studies of Bose polarons in all physical dimensions: 3D, 2D, and 1D. Some examples of methods developed to tackle the 2D case with short-range interactions include the Fröhlich polaron model, which was treated by the Feynman variational method [20] and by perturbation theory [21], a truncated-basis variational approach [22–24], diffusion quantum Monte-Carlo calculations [17, 25], functional renormalization group theory [26], a T -matrix approximation [27], and variational mean-field (coherent-state) methods, both static and dynamic [28–30].

The problem of a Bose polaron in a dense excitonic system with realistic interaction laws [such as Eq. (S11)] has received much less attention. Some nonperturbative calculations within the hypernetted chain method have been reported [16]. Unfortunately, those results are not directly relevant for the present study because of a different geometry of the problem (an e-h quadrilayer instead of the bilayer).

In general, the goal is to find the dispersion $E = E(P)$ of the Bose polarons, which is determined by the peaks of the spectral function

$$A_{\text{DX}}(P, E) = -2 \text{Im} G_{\text{DX}}(P, E), \quad (\text{S25})$$

where

$$\begin{aligned} G_{\text{DX}}(P, E) &= -i \int_0^\infty dt e^{iEt/\hbar} \langle [a_{\text{P}}(t), a_{\text{P}}^\dagger(0)] \rangle \\ &\equiv \left[E - \frac{\hbar^2 P^2}{2m_{\text{DX}}} - \Sigma(P, E) + i0^+ \right]^{-1} \end{aligned} \quad (\text{S26})$$

is the retarded Green's function of the impurity (in our case, a DX) and $a_{\mathbf{k}}(a_{\mathbf{k}}^\dagger)$ is the impurity creation (annihilation) operators. To analyze the polaron resonances probed in optical experiments it is sufficient to consider $P = 0$ only, and so we suppress the momentum argument P in the formulas below.

Within the T -matrix method the self-energy of the Bose polaron is given by

$$\Sigma(E) = nT(E), \quad (\text{S27})$$

which is similar to Eq. (S9). A formula for the T -matrix of a weakly-coupled BEC of spinless bosons has been proposed by Raith and Schmidt (RS) [31]. In our notations, it looks as follows:

$$T(E) = \frac{\widetilde{V}}{1 - L_{\text{RS}}(E)\widetilde{V}}, \quad (\text{S28})$$

$$L_{\text{RS}}(E) = \frac{1}{\Omega} \sum_{|\mathbf{k}| < \Lambda} \frac{u_{\mathbf{k}}^2}{E - \omega_{\mathbf{k}} - \varepsilon_{\text{DX},\mathbf{k}}}, \quad (\text{S29})$$

where

$$\omega_{\mathbf{k}} = \sqrt{\varepsilon_{\mathbf{k}}^2 + 2\zeta\varepsilon_{\mathbf{k}}}, \quad (\text{S30})$$

$$u_{\mathbf{k}} = \frac{1}{2} \left(\sqrt{\frac{\omega_{\mathbf{k}}}{\varepsilon_{\mathbf{k}}}} + \sqrt{\frac{\varepsilon_{\mathbf{k}}}{\omega_{\mathbf{k}}}} \right) \quad (\text{S31})$$

are the Bogoliubov excitation energies and coherence factors. RS derived Eq. (S28) by summing a subset of ladder diagrams. Identical expressions have been also obtained within the truncated-basis approach [24]. Focusing on the equal-mass case $m_{\text{DX}} = m$, it is easy to show analytically that $L_{\text{RS}}(E) = L(E)$ [cf. Eq. (S15)]. Hence, these theories predict, surprisingly, that $T(E)$ is no different from the vacuum two-body T -matrix given by Eq. (S14). Therefore, to adapt this approach to the spinful case, we can use our results from Sec. VB and try

$$T(E) = \frac{3}{4} T^a(E) + \frac{1}{4} T^s(E), \quad (\text{S32})$$

assuming equal concentrations of all IX spin states.

In our model the triplet term $T^a(E) = \widetilde{V}_x$ is energy-independent, and so it shifts the self-energy by a fixed amount

$$\Delta\Sigma = \frac{3}{4} \widetilde{V}_x n, \quad (\text{S33})$$

which is equivalent to a shift of the DX chemical potential. This suggests an improved approximation

$$\begin{aligned} \Sigma(E) &= \Delta\Sigma + \frac{1}{4} nT^s(E - \Delta\Sigma) \\ &= \Delta\Sigma + \frac{\pi\hbar^2}{m} n \left[\ln \left(-\frac{E_{\text{XX}}}{E - \Delta\Sigma} \right) \right]^{-1}. \end{aligned} \quad (\text{S34})$$

(We used $2\mu = m$ in the denominator assuming $m_{\text{DX}} = m$.) The resultant spectral function $A_{\text{DX}}(E)$ has peaks at energies that solve the equation $E = \text{Re} \Sigma(E)$. The higher-energy solution is the RBP:

$$E_{\text{RBP}} \simeq \Delta\Sigma(n) + \frac{\pi\hbar^2}{m} \frac{n}{\ln(1/na_{\text{XX}}^2)}, \quad n \ll a_{\text{XX}}^{-2}. \quad (\text{S35})$$

This equation is different from those previously derived for spinless bosons [17, 21] in two aspects. One is the addition of $\Delta\Sigma(n)$, the other is the extra factor of 1/4 in the

second term. Both differences originate from the electron spin. The ‘repulsive’ nature of the RBP is manifested in its energy increase with n , which is due to the positive sign of $\text{Re } T(E)$. Note that $\text{Re } T^s(E) > 0$ at $-E_{XX} < E < E_{XX}$, which can be thought of as a ‘level repulsion’ at energies above the bound-state resonance. At the face value, Eq. (S35) predicts a diverging E_{RBP} at $n \rightarrow 1/a_{XX}^2$. This is referred to as the strong coupling regime for the Bose polaron. In fact, at large n , this solution of the equation $E = \text{Re } \Sigma(E)$ has the asymptotic behavior $E_{\text{RBP}} \simeq \Delta\Sigma(n) + E_{XX}$.

The lower-energy solution corresponds to the ABP. It depends on n as

$$E_{\text{ABP}} \simeq \Delta\Sigma(n) - \begin{cases} \frac{\pi\hbar^2}{m}n + E_{XX}, & n \ll a_{XX}^{-2}, \\ \frac{\pi\hbar^2}{m} \frac{n}{\ln(na_{XX}^2)}, & n \gg a_{XX}^{-2}. \end{cases} \quad (\text{S36a})$$

Note that Eq. (S36b) is the same as Eq. (S35). However, the ‘reduced energy’ $E_{\text{ABP}} - \Delta\Sigma(n)$ now decreases with n , which is a signature of DX-IX attraction.

The DX spectral function computed numerically from Eqs. (S25), (S26), (S33), and (S34) is plotted in Fig. S5(a). To regularize the δ -function-like ABP peak we added a damping constant $-i\Gamma$ to $\Delta\Sigma$. Both the ABP and RBP energies increase with IX density n , in a qualitative agreement with the experiment. The rate of increase is however somewhat smaller. The distance $\Delta_{\text{ABP-RBP}}$ between the two peaks as a function of n is shown in Fig. S5(b). The starting point, $\Delta_{\text{ABP-RBP}} = E_{XX}$ is in a good agreement with the measured value, the subsequent rate of increase is about twice slower. In the context of the polaron problem, the integrated weight (or so-called quasi-particle residue) of the spectral peaks is often discussed. As shown in Fig. S5(c), the spectral weight is steadily transferred from the RBP to to ABP as n increases, which is also apparent from Fig. S5(a). Finally, in Fig. S5(d) we present the evolution of the peak widths. The ABP peak maintains the constant width equal to Γ (which we added by hand). The RBP peak widens with n . This widening originates from the imaginary part of the T -matrix and represents collisional broadening of an unbound DX being scattered by IXs.

The described T -matrix theory is certainly an approximation. It does not capture several additional effects as follows. In Sec. VB we suggested that the ABP is essentially a dimer. In fact, the ABP can still be dressed with Bogoliubov-like excitations of the medium, i.e., density oscillations localized near the dimer. Such excitations would produce spectral weight above the lowest-energy ABP state. This spectral weight can be substantial. In the strong-coupling polaronic regime, it may even exceed that of the ground ABP state. Conversely, for the RBP, which is a metastable state, these local modes typically have negative energies, producing spectral lines below the main RBP peak [32]. Therefore, a non-negligible absorption can be present everywhere in between ABP and

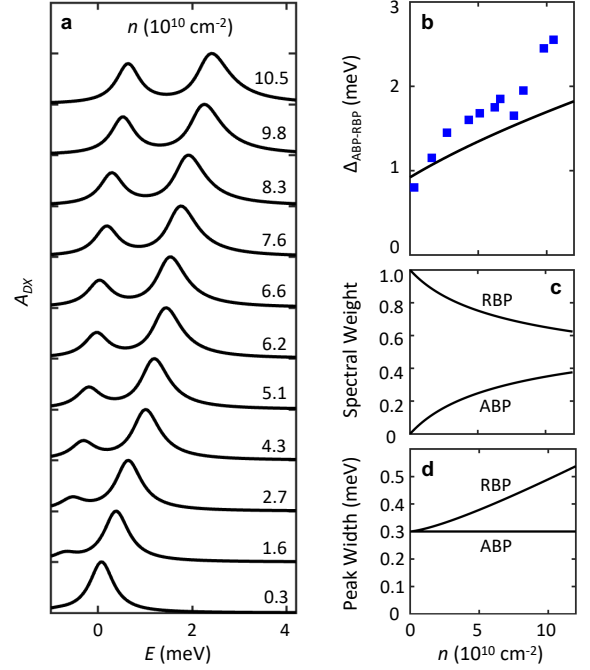


FIG. S5. (a) Calculated DX spectral function for different n using $E_{XX} = (0.96+0.88)/2 = 0.92$ meV and damping $\Gamma = 0.3$ meV. The lower-energy and higher-energy peaks correspond to the ABP and RBP, respectively. (b) The ABP-RBP energy splitting deduced from panel (a) (line). The squares are experimental data from Fig. 2 of the main text. (c) ABP and RBP spectral weight vs. n . (d) ABP and RBP peak width vs. n .

RBP energies.

VII. A PHENOMENOLOGICAL T-MATRIX MODEL

The T -matrix theory of Sec. VI gives a qualitative but not quantitative agreement with the experiment. It is also not fully satisfactory for several conceptual reasons. First, Eq. (S29) disagrees with the perturbation theory formula [21, 33]

$$\Sigma = n\tilde{V} + \frac{n\tilde{V}^2}{\Omega} \sum_{|\mathbf{k}| < \Lambda} \frac{\varepsilon_{\mathbf{k}}}{\omega_{\mathbf{k}}} \frac{1}{E - \omega_{\mathbf{k}} - \varepsilon_{\text{DX},\mathbf{k}}} \quad (\text{S37})$$

already in the order $O(\tilde{V}^2)$ unlike other theoretical calculations [28, 32], which do agree with Eq. (S37). The perturbation theory indicates that the response of the BEC to the impurity is suppressed at energy scales below ζ where it behaves as a fairly ‘rigid’ medium with excitation energies much larger than the bare particle energies, $\omega_{\mathbf{k}} \gg \varepsilon_{\mathbf{k}}$. In contrast, the RS theory [31] and the truncated-basis method [24] (at the single-Bogoliubov-excitation level) predict that the interaction among host bosons practically do not affect the response of the BEC. (If $m_{\text{DX}} = m$, there is no difference at all, see Sec. VI.)

Second, as explained in Sec. V A, the IX system is strongly correlated, so diagrammatic approaches, perturbative or otherwise, are uncontrolled. In the same vein, formulas like Eqs. (S29) or (S37) assume unrealistic (extremely short-range) IX-IX interaction law.

It may therefore be prudent to retain only the basic properties of the theory outlined in the previous section and make phenomenological assumptions about all quantities that are difficult to compute reliably. Returning to Eq. (S34), we can argue that it represents splitting of the self-energy into a non-singular part with a slow E -dependence and a singular part that has a pole at some energy

$$E_{\text{ABP}}^{(0)} = -E_{\text{XX}} + ng_2. \quad (\text{S38})$$

This leads us to the model introduced in the main text:

$$T(E) = g_1 + g_3 \frac{E_{\text{XX}}}{E - E_{\text{ABP}}^{(0)}}. \quad (\text{S39})$$

As stated therein, this model predicts the polaron ener-

gies

$$E_{\text{ABP,RBP}} = \frac{1}{2} (2ng_1 - E_{\text{XX}} \pm \Delta_{\text{ABP-RBP}}), \quad (\text{S40})$$

$$\Delta_{\text{ABP-RBP}} = \left(E_{\text{XX}}^2 + 4ng_3 E_{\text{XX}} \right)^{1/2}, \quad (\text{S41})$$

which agree fairly well with the measured peak energies. Here we already set $g_1 = g_2$ because it is physically reasonable if the DX-IX biexciton is weakly bound and because it helps to reduce the number of phenomenological parameters. This model also predicts the polaron spectral weights (quasiparticle residues)

$$Z_{\text{ABP,RBP}} = \frac{1}{1 - (d\Sigma/dE)} = \frac{1}{2} \pm \frac{1}{2} \frac{E_{\text{XX}}}{\Delta_{\text{ABP-RBP}}}, \quad (\text{S42})$$

which depend on n similar to what is shown in Fig. S5(c).

We can use the formulas of Secs. V B and VI to crudely estimate g_1 and g_3 . For the case of g_1 , we take $ng_1 = \Delta\Sigma(n)$, i.e., $g_1 = (3/4)\tilde{V}_x$, see Eq. (S33). For g_3 , we use Eqs. (S17) and (S32) to obtain $g_3 = \pi\hbar^2/2\mu$. These are the estimates quoted in the main text, e.g., $g_1 = 0.21 \times 10^{-10} \text{ meV cm}^2$ for hh. It is also possible to extract g_1 from the measured peak positions by fitting them to Eqs. (S40) and (S41). Doing so for the hh points in Fig. 2b, we obtained $g_1 = 0.34 \times 10^{-10} \text{ meV cm}^2$. A better physical understanding of these parameter values and other spectral characteristics of the excitonic Bose polarons warrants future experimental and theoretical work.

-
- [1] A. T. Hammack, N. A. Gippius, S. Yang, G. O. Andreev, L. V. Butov, M. Hanson, and A. C. Gossard, *J. Appl. Phys.* **99**, 066104 (2006).
 - [2] D. J. Choksy, E. A. Szwed, L. V. Butov, K. W. Baldwin, and L. N. Pfeiffer, *Nature Physics* **19**, 1275 (2023).
 - [3] G. Bastard and J. Brum, *IEEE J. Quantum Electron.* **22**, 1625 (1986).
 - [4] F. T. Vasko and A. V. Kuznetsov, *Electronic States and Optical Transitions in Semiconductor Heterostructures*, Graduate Texts in Contemporary Physics (Springer, New York, 1998).
 - [5] K. Sivalertporn, L. Mouchliadis, A. L. Ivanov, R. Philp, and E. A. Muljarov, *Phys. Rev. B* **85**, 045207 (2012).
 - [6] C. Y.-P. Chao and S. L. Chuang, *Phys. Rev. B* **43**, 6530 (1991).
 - [7] K. Varga and Y. Suzuki, *Phys. Rev. C* **52**, 2885 (1995).
 - [8] A. D. Meyertholen and M. M. Fogler, *Phys. Rev. B* **78**, 235307 (2008).
 - [9] M. M. Fogler, L. V. Butov, and K. S. Novoselov, *Nature Communications* **5**, 4555 (2014).
 - [10] M. Schick, *Physical Review A* **3**, 1067 (1971).
 - [11] V. N. Popov, *Theoretical and Mathematical Physics* **11**, 565 (1972).
 - [12] G. E. Astrakharchik, J. Boronat, J. Casulleras, I. L. Kurbakov, and Y. E. Lozovik, *Physical Review A* **75**, 063630 (2007).
 - [13] G. E. Astrakharchik, J. Boronat, J. Casulleras, I. L. Kurbakov, and Y. E. Lozovik, *Physical Review A* **79**, 051602 (2009).
 - [14] H. Haug and S. Schmitt-Rink, *Progress in Quantum Electronics* **9**, 3 (1984).
 - [15] C. Schindler and R. Zimmermann, *Phys. Rev. B* **78**, 045313 (2008).
 - [16] C. Xu and M. M. Fogler, *Phys. Rev. B* **104**, 195430 (2021).
 - [17] L. A. Peña Ardila, G. E. Astrakharchik, and S. Giorgini, *Physical Review Research* **2**, 023405 (2020).
 - [18] G. Guijarro, G. E. Astrakharchik, J. Boronat, B. Bazak, and D. S. Petrov, *Physical Review A* **101**, 041602 (2020).
 - [19] S. Schmitt-Rink, D. S. Chemla, and D. A. B. Miller, *Adv. Phys.* **38**, 89 (1989).
 - [20] W. Casteels, J. Tempere, and J. T. Devreese, *Physical Review A* **86**, 043614 (2012).
 - [21] V. Pastukhov, *Journal of Physics B: Atomic, Molecular and Optical Physics* **51**, 155203 (2018).
 - [22] J. Levinsen, F. M. Marchetti, J. Keeling, and M. M. Parish, *Physical Review Letters* **123**, 266401 (2019).
 - [23] I. Amelio, N. D. Drummond, E. Demler, R. Schmidt, and A. Imamoglu, *Phys. Rev. B* **107**, 155303 (2023).
 - [24] Y. Nakano, M. M. Parish, and J. Levinsen, *Physical Review A* **109**, 013325 (2024).
 - [25] E. Akaturk and B. Tanatar, *International Journal of Modern Physics B* **33**, 1950238 (2019).
 - [26] F. Isaule, I. Morera, P. Massignan, and B. Juliá-Díaz, *Phys-*

- ical Review A **104**, 023317 (2021).
- [27] L. F. Cárdenas-Castillo and A. Camacho-Guardian, *Atoms* **11**, 3 (2022).
- [28] O. Hryhorchak, G. Panochko, and V. Pastukhov, *Journal of Physics B: Atomic, Molecular and Optical Physics* **53**, 205302 (2020).
- [29] G. Panochko and V. Pastukhov, *Atoms* **10**, 19 (2022).
- [30] T. Shi, E. A. Demler, and et al., unpublished.
- [31] S. P. Rath and R. Schmidt, *Phys. Rev. A* **88**, 053632 (2013).
- [32] Y. E. Shchadilova, R. Schmidt, F. Grusdt, and E. Demler, *Physical Review Letters* **117**, 113002 (2016).
- [33] R. S. Christensen, J. Levinsen, and G. M. Bruun, *Physical Review Letters* **115**, 160401 (2015).